

RSC Advances



This is an *Accepted Manuscript*, which has been through the Royal Society of Chemistry peer review process and has been accepted for publication.

Accepted Manuscripts are published online shortly after acceptance, before technical editing, formatting and proof reading. Using this free service, authors can make their results available to the community, in citable form, before we publish the edited article. This *Accepted Manuscript* will be replaced by the edited, formatted and paginated article as soon as this is available.

You can find more information about *Accepted Manuscripts* in the [Information for Authors](#).

Please note that technical editing may introduce minor changes to the text and/or graphics, which may alter content. The journal's standard [Terms & Conditions](#) and the [Ethical guidelines](#) still apply. In no event shall the Royal Society of Chemistry be held responsible for any errors or omissions in this *Accepted Manuscript* or any consequences arising from the use of any information it contains.

1 **A Novel High Conductive Ferroferric Oxide/Porous Carbon Nanofibers**
2 **Composites Prepared by Electrospinning as Anode Materials for High**
3 **Performance Li-ion Batteries**

4 Shoupu Zhu, Ming Chen*, Jing Sun, Jingwen Liu, Tian Wu, Haiming Su, Shanshan Qu,
5 Yongjuan Xie, Shishuang Wang, Xun Su and Guowang Diao*

6 College of Chemistry and Chemical Engineering, Yangzhou University, Yangzhou
7 225002, P. R. China

8 Key Laboratory of Environmental Materials & Environmental Engineering of Jiangsu
9 Province, Yangzhou 225002, Jiangsu, P. R.China

10 **Abstract:** In this paper, ferroferric oxide (Fe_3O_4) nanoparticles/porous carbon nanofibers
11 ($\text{Fe}_3\text{O}_4/\text{PCNFs}$) composites were successfully fabricated by electrospinning and subsequent
12 calcinations. The composites were characterized by X-ray diffraction, thermogravimetric
13 analysis, scanning electron microscopy and transmission electron microscopy to analyze the
14 structure, composition and morphology. The electrochemical performance was evaluated by
15 coin-type cells versus metallic lithium. The results indicated that $\text{Fe}_3\text{O}_4/\text{PCNFs}$ composites
16 exhibited high reversible capacity and good capacity retention. The discharge capacity
17 maintained $717.2 \text{ mA h g}^{-1}$ at 0.5 A g^{-1} after 100 cycles. The excellent performances of
18 $\text{Fe}_3\text{O}_4/\text{PCNFs}$ composites are attributed to good crystallinity and uniformly dispersive Fe_3O_4
19 nanoparticles, and porous carbon shell with high conductivity. The carbon coating buffered
20 the tremendous volumetric changes between Fe_3O_4 nanoparticles and Fe atoms in the
21 charge/discharge processes and kept the structure integrity of Fe_3O_4 nanoparticles. Porous
22 carbon nanofibers prepared by unique calcination process improved the conductivity of
23 composites and provided free space for migration of lithium ions. The preparation of strategy
24 is expected to be applied to the preparation of other transition metal oxides materials as

* Corresponding author. Tel.: +86 514 87975436; fax: +86 514 87975244. E-mail address: gwldiao@yzu.edu.cn
(G. Diao), chenming@yzu.edu.cn (M. Chen).

25 superior anode materials for lithium-ion batteries.

26 **Keywords:** Porous nanofiber; Fe₃O₄ nanoparticles; Electrospinning; Hybrid anode materials;
27 Li-ion battery

28

29 1 INTRODUCTION

30 Haze and greenhouse effect have become severe challenges to environment, which are
31 closely connected to excessive use of fossil fuels ^[1-3]. Rechargeable lithium ion batteries are
32 tools of energy exchange between chemistry energy and electric energy ^[3-4], which can store
33 energy from clean energy ^[5]. As rechargeable lithium ion batteries have the characteristics of
34 high energy density, long lifespan, environment friendly and fast charge-discharge rates ^[6-7],
35 they have been widely applied to mobile phones, digital cameras and laptops, etc ^[7]. But
36 hybrid electric vehicles and electric vehicles require Li-ion batteries to have higher energy
37 density and rate capability ^[3,8] to match the performance of internal combustion vehicles ^[3].

38 Natural graphite seems to be the most promising candidate for the anode material in
39 lithium-ion batteries because of its numerous advantages ^[9,10]. Graphite and graphitized
40 carbon as anode materials in lithium-ion batteries have been used in many commercial
41 products on the market ^[9]. Modification of carbonaceous anode materials which has been a
42 research focus ^[11] can greatly improve materials' electrochemical performance. Composites
43 of carbon nanomaterials and sulfides ^[12-16]/metal oxides ^[17-21] have been intensively studied
44 for efficient energy storage. Transition metal oxides (MO) (Fe₂O₃, Fe₃O₄, NiO, CoO, Co₃O₄,
45 Cu₂O, CuO, RuO₂ and Cr₂O₃ *etc.*) have much higher theoretical capacities (~1000 mA h g⁻¹)
46 than graphite based on the conversion between MO and M ^[17]. But pure transition metal
47 oxides as anodes in lithium ion batteries often have poor cycling performance owing to the
48 collapse of lattice structure of the original crystal over several discharge/charge cycles as the
49 tremendous volume changes ^[18-19]. A number of research methods about transition metal

50 oxides as anodes in lithium ion batteries have been carried out to improve the deficiency and
51 obtained excellent electrochemical performance by constructing nanostructured materials,
52 hollow nanostructures, hybrid nanostructures, etc. Carbon coating is the most widely used
53 modification techniques for transition metal oxides. On the one hand, carbon coating on the
54 surfaces of metal oxide nanoparticles can reduce the side reactions of solid electrolyte
55 interface (SEI) at the interface between metal oxide and electrolyte ^[19]. On the other hand,
56 good electrical conductivity of carbon can make up for the poor conductivity of metal oxides
57 and promote the electron transport. What's more, carbon coating as elastic buffer
58 layers/supports ^[20] can confine the position of metal oxides and prevent the agglomeration
59 and cracking of crystal structures which can enhance the cycle stability of electrode. In
60 addition, nanostructured electrode materials have some special characteristics, such as large
61 proportion of surface atoms, small size, etc. which lead to higher electrode/electrolyte contact
62 area, shorter path lengths for Li⁺ transport and higher charge/discharge rates^[21]. So carbon
63 coating nanostructured metal oxides as anodes in lithium ion batteries would strengthen the
64 cycle stability and improve the high-rate charge-discharge performance. Iron oxides have the
65 characteristics of low price, environment-friendliness and abundant resources, which make
66 them charming anodes for high performance lithium-ion batteries ^[20].

67 A lot of Fe₃O₄/carbon nanocomposites ^[22-25] and Fe₂O₃/carbon nanocomposites ^[26-28]
68 have been fabricated and detected as electrode materials for lithium ion batteries. Carbon
69 coating iron oxides nanoparticles can form 0 D nanospheres ^[29-30], 1 D nanowires ^[31-32], 2 D
70 nanoflakes ^[33-34] and 3 D structures of porous carbon foam loading iron oxide ^[35-36].
71 Electrospinning is one of the carbon coating methods and has been used to fabricate 1 D
72 hybrid carbon coating iron oxides nanofibers composites ^[37-41], 1 D iron oxides nanofibers
73 ^[42-43] and 1 D carbon nanofibers for Li ion batteries ^[44-45]. The method can embed the iron
74 oxides into a conductive carbon by subsequent heat treatment and enhance the

75 electrochemical properties effectively. Zhang, X. ^[37] fabricated Fe₂O₃-carbon composite
76 nanofibers as durable anode materials for lithium ion batteries. The cell exhibits a reversible
77 capacity of 820 mA h g⁻¹ at a current rate of 0.2 C even after 100 cycles. Chaudhari, S. ^[42]
78 synthesized hollow-structured α -Fe₂O₃ nanofibers by a simple electrospinning technique and
79 subsequent calcination at 500 °C for 4 h in air. The hollow fibers anodes obtained a high
80 reversible capacity of 1293 mA h g⁻¹ at a current density of 60 mA g⁻¹ (0.06 C). Kim, C. ^[44]
81 fabricated high-purity carbon nanofiber webs by combination of electrospinning 10 wt. %
82 polyacrylonitrile (PAN) polymer - dimethyl formamide (DMF) solution and thermal
83 treatments. Nanofiber webs thermally treated at 1000 °C in Ar have the highest reversible
84 capacity of 450 mA h g⁻¹ than that of 700 °C or 2800 °C at a discharge current density of 30
85 mA g⁻¹.

86 Here, 1D Fe₃O₄ nanoparticles/porous carbon nanofibers (Fe₃O₄/PCNFs) composites are
87 fabricated by electrospinning a 10 wt. % PAN and 3 wt. % Fe(acac)₃ dissolving in DMF
88 solution and subsequent thermal treatments (Fig. 1). The innovative thermal treatments are
89 made up of four calcination processes for the first time. Firstly, the electrospun nanofibers
90 were pre-oxidized at 250 °C in air to maintain their morphologies. Secondly, carbonization
91 was proceeded at 1000 °C in argon to obtain high conductive graphitized carbon. Thirdly,
92 oxidation was continued at 400 °C in blowed air to change Fe atoms and Fe C compounds
93 into iron oxides and remove some graphitized carbon of the nanofibers to form pore
94 structures. Carbothermic reduction was finally proceeded at 500 °C in Ar to change Fe₂O₃
95 nanoparticles into high conductive Fe₃O₄ nanoparticles with better crystal structures and
96 further more increase porosity of the nanofibers. What should be noted is that the flow rate of
97 air and calcinating equipment have very significant effects on content of carbon and types of
98 iron oxides in the third calcination process. The excellent electrochemical properties of the
99 novel high conductive Fe₃O₄/PCNFs composites anode is evident from the high capacity of

100 717.2 mA h g⁻¹ after 100 cycles at 0.5 A g⁻¹.

101 2 EXPERIMENTAL SECTION

102 2.1 Fabrication of Fe₃O₄/PCNFs Composites

103 PAN with 150,000 average molecular weight was purchased from Aladdin. Analytic
104 grade ferric acetylacetonate (Fe(acac)₃) and DMF were obtained from Sinopharm Chemical
105 Reagent Co.,Ltd. All the reagents were not further purified before using.

106 In a typical process, 1 g PAN and 0.3 g Fe(acac)₃ were added into 8.70 g DMF and
107 formed a 10 g mixture, followed by vigorous stirring at room temperature for at least 24 h.
108 The obtained homogeneous dispersion was used as the Fe₃O₄/PCNFs composites precursor
109 solution for electrospinning. The precursor solution was loaded into a 10 mL plastic syringe
110 connected to a blunt-tip needle with a inner diameter of 0.33 mm. The distance between the
111 needle tip and collector is 15 cm. The injection flow rate of the solution was set to 0.1 mm
112 min⁻¹ (about 1 mL h⁻¹) driven by a pump. A total voltage power of 15 kV was applied
113 between the needle (12 kV) and a plate (-3 kV) covered with aluminum foil. Electrospinning
114 was proceeded with a commercial setup (Beijing Ucalery Technology Development Co., Ltd,
115 SS-2535DC). The environmental humidity of electrospinning was 45 ± 10 %, and temperature
116 25 ± 5 °C. The electrospun nanofibers were firstly preoxidized at 250 °C for 120 min with a
117 heating rate of 1 °C min⁻¹ in air atmosphere in a tube furnace (Hefei Ke Jing Materials
118 Technology Co., Ltd., OTF-1200xΦ50) to keep fibrous morphology, and then carbonized at
119 1000 °C for 120 min with a heating rate of 5 °C min⁻¹ in argon atmosphere to obtain high
120 conductive graphitized carbon. Then the composite nanofibers were calcined at 400 °C for 3
121 h with a heating rate of 5 °C min⁻¹ in air atmosphere to obtain the Fe₂O₃ and Fe₃O₄
122 nanoparticle-loaded porous carbon nanofibers (Fe_xO_y/PCNFs) composites. It should be noted
123 that the flow of air and the calcination time both have a profound influence on the
124 compositions and morphology of the Fe_xO_y/PCNFs composites because it is likely that

125 graphitized carbon is completely oxidized to CO_2 and Fe_xO_y transforms into pure Fe_2O_3 by
 126 much longer time calcination and bigger air flow rate at $400\text{ }^\circ\text{C}$ in air. At last, $\text{Fe}_3\text{O}_4/\text{PCNFs}$
 127 composites were prepared by further calcination at $500\text{ }^\circ\text{C}$ for 2 h with a heating rate of $5\text{ }^\circ\text{C}$
 128 min^{-1} in argon atmosphere.

129 For comparison, homogeneous dispersion containing 1.00 g PAN and 9.00 g DMF was
 130 also prepared, and then proceeded electrospinning and calcination with the same processes. In
 131 addition, the preoxidized nanofibers were calcined at $700\text{ }^\circ\text{C}$ or $900\text{ }^\circ\text{C}$ in Ar to
 132 observe electrical conductivity of calcinated nanofibers at different calcination temperature.
 133 For ease of description, the above products were renamed in this article as follows.

134 **Table 1** Renaming of various products with different composition and calcination
 135 temperature.

Samples	Fe(acac) ₃ g	PAN g	DMF g	Temp (atm) First	Temp (atm) Second	Temp (atm) Third	Temp (atm) Last
PAN0-250	0.00	1.00	9.00	250 °C (air)	—	—	—
PAN0-700	0.00	1.00	9.00	250 °C (air)	700 °C (Ar)	—	—
PAN0-900	0.00	1.00	9.00	250 °C (air)	900 °C (Ar)	—	—
PAN0-1000	0.00	1.00	9.00	250 °C (air)	1000 °C (Ar)	—	—
PAN0-400	0.00	1.00	9.00	250 °C (air)	1000 °C (Ar)	400 °C (air)	—
PAN0-500	0.00	1.00	9.00	250 °C (air)	1000 °C (Ar)	400 °C (air)	500 °C (Ar)
PAN3	0.30	1.00	8.70	—	—	—	—
PAN3-250	0.30	1.00	8.70	250 °C (air)	—	—	—
PAN3-1000	0.30	1.00	8.70	250 °C (air)	1000 °C (Ar)	—	—
PAN3-400	0.30	1.00	8.70	250 °C (air)	1000 °C (Ar)	400 °C (air)	—
PAN3-500	0.30	1.00	8.70	250 °C (air)	1000 °C (Ar)	400 °C (air)	500 °C (Ar)

151 Comment: Temp = Temperature, atm = atmosphere.

152 2.2 Materials characterizations

153 The crystal structures of as-prepared materials were characterized using powder X-ray
 154 diffraction(XRD) on a D8 Advanced with lynxEye and SolX (Bruker AXS, WI, USA) with a
 155 Cu-K α radiation source between 10° and 80° . The morphologies were characterized using a
 156 field-emission scanning electron microscopy (SEM) (S-4800 II, Hitachi, Japan) and a field

157 emission transmission electron microscopy (TEM) (Tecnai 12, Philips, Holland) in the Test
158 Center of Yangzhou University. A SEM (Zeiss Supra™ 55, Sapphire Carl Zeiss Group,
159 Germany) and a TEM (JEM-2100, JEOL, Japan) in College of Chemistry and Chemical
160 Engineering of Yangzhou University were also used to characterized the morphologies.
161 High-resolution TEM (HRTEM) and high-angle annular dark-field scanning transmission
162 electron microscopy (HAADF-STEM) were conducted using a FEI Tecnai G2 F30 STWIN
163 (USA) operating at 200 kV. Thermogravimetric analysis (TGA) (Pyris 1 TGA, PerkinElmer,
164 USA) was performed in air atmosphere up to 800 °C at a heating rate of 10 °C min⁻¹. Raman
165 spectra was conducted with a laser Raman spectrometer (In Via, Renishaw, UK) at the 532
166 nm wavelength. The magnetic measurements of PAN3-400 and PAN3-500 were performed
167 on a vibrating sample magnetometer (VSM) (EV7, ADE, USA). The electrical conductivities
168 of different pure carbon nanofibers were measured by a direct volt-ampere method (SZT-2A,
169 Suzhou Tong-Chang electronics company Ltd, CHN). Nitrogen physisorption–desorption
170 measurements at 100 °C were performed by a surface area and porosity analyzer (ASAP 2020
171 HD88, Micromeritics, USA). Brunauer–Emmett–Teller (BET) analyses were done by
172 software to characterize surface properties of porous carbon nanofibers. X-Ray photoelectron
173 spectroscopy (XPS) measurements were conducted with an Al K α (1486.8 eV) X-ray source
174 (ESCALAB 250Xi, Thermo Fisher Scientific, USA).

175 **2.3 Electrochemical measurements**

176 The calcined flexible PAN0-500, PAN3-400 and PAN3-500 mats were cut into
177 electrodes with size Φ 16 mm, which were assembled into lithium ion batteries by attaching
178 onto a current collector copper foil with 10 wt. % PVDF which dissolved in
179 1-methyl-2-pyrrolidone (NMP) as binder. The electrodes were first dried in a
180 vacuum drying oven at 80 °C for 12 h. The PAN0-500, PAN3-400 or PAN3-500 electrode
181 was about 2 mg. Then coin cells were assembled with metallic lithium as the

182 counter/reference electrode, 1 M LiPF₆ in ethylene carbonate (EC), diethyl carbonate (DMC)
183 and ethylmethyl carbonate (EMC) (1:1:1 by volume) as electrolyte, and Celgard 2400
184 polypropylene as separator in an high-purity argon-filled glovebox (VAC-Omni, OMNI-LAB,
185 Vacuum atmospheres company, CA). Cyclic voltammetry (CV) measurements were
186 performed using an electrochemical workstation (CHI660 E, Chenghua, CHN) at a scan rate
187 of 0.0001 V s⁻¹ between 0.01 and 3.0 V. Galvanostatic charge (lithium extraction) and
188 discharge (lithium insertion) cycling of the cells were carried out using a battery test system
189 (CT-3008W, Xinwei, CHN) at the different current densities of 0.05, 0.1, 0.2, 0.5 and 1.0 A
190 g⁻¹ between 0.01 and 3 V (vs. Li⁺/Li) to observe ratio performance, and at the current density
191 of 0.5 A g⁻¹ to study cycle stability. Electrochemical impedance spectroscopic
192 (EIS) measurements were carried out on an electrochemical analyzer (Autolab, Ecochemie,
193 NL). All the current densities and capacities in this study were calculated on the basis of the
194 weight of integral maps.

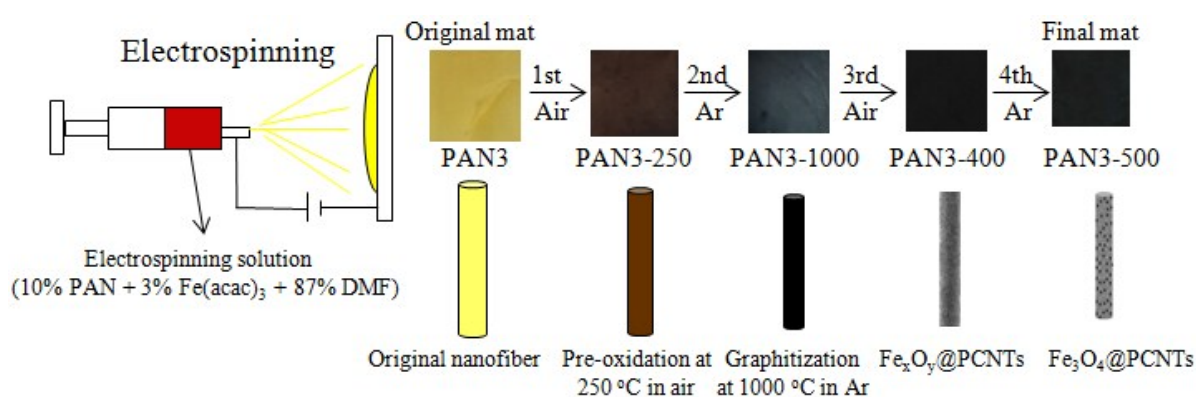
195 Finally, the morphology of PAN3-500 anode was observed by S-4800 II SEM and
196 Tecnai 12 field emission TEM after 100 charge/discharge cycles at 0.5A g⁻¹.

197 **3 RESULTS AND DISCUSSION**

198 **3.1 Preparation process**

199 The overall synthesis procedures of Fe₃O₄/PCNFs composites are schematically
200 illustrated in Fig. 1. PAN and Fe(acac)₃ were dissolved in DMF forming uniform viscous
201 reddish-brown electrospinning solution by stirring 24 h. And electrospinning was carried out
202 using above conditions in experimental section. The original electrospinning nanofibers
203 (PAN3) films are yellow. Wide brown slices (PAN3-250) are obtained by pre-oxidation of
204 PAN3 films at 250 °C in air. Black graphitized nanofibers (PAN3-1000) composites are
205 prepared by calcination of PAN3-250 films at 1000 °C in Ar. Black porous graphitized carbon
206 coating Fe_xO_y nanofibers (PAN3-400) sheets are gotten by calcinating PAN3-1000 at 400 °C

207 in air. At last, black $\text{Fe}_3\text{O}_4/\text{PCNFs}$ (PAN3-500) compounds are gained by calcinating
 208 PAN3-400 in Ar at 500 °C. The pieces have continuous macroscopic area shrinkages by
 209 pre-oxidation and graphitization, which can be demonstrated from the microscopic
 210 characterizations of SEM and TEM images below. PAN3-400 flakes have obvious weight
 211 loss and become more fluffy than PAN3-1000 pieces. A portion of carbon should be oxidized
 212 to CO_2 at 400 °C and form a large amount of pores in air atmosphere, which can be
 213 demonstrated by the BET results of PAN0-1000 and PAN0-400 as shown in Fig. 2.

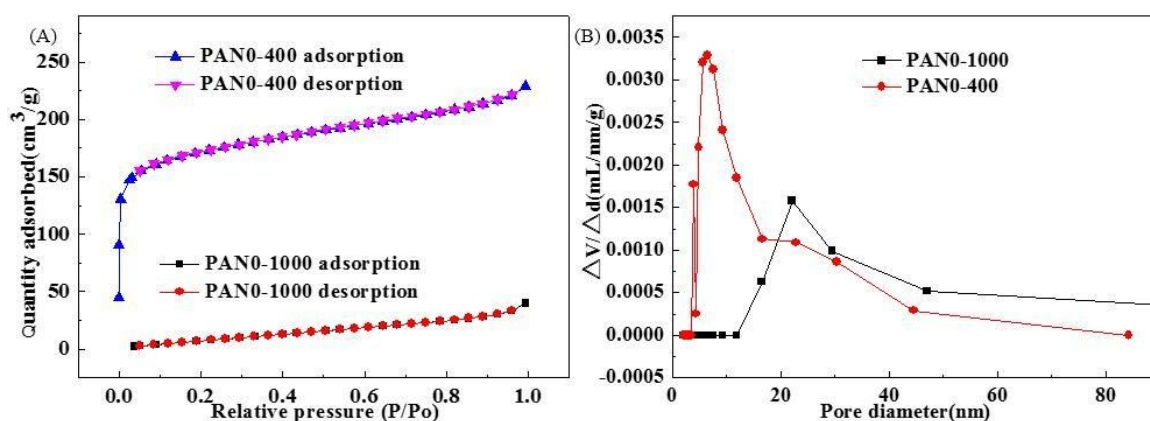


214
 215 **Fig. 1** Schematic illustration of the process of electrospinning and products of different
 216 calcination conditions.

217 3.2 Materials characterization

218 It is well known that high temperature is advantageous to the graphitization of
 219 nanofibers. The pure PAN0-250 was calcinated at the temperature of 700, 900 and 1000 °C
 220 under Ar. Table 2 shows the conductivities of carbon nanofibers with the various calcination
 221 temperatures and BET results of PAN0-1000 and PAN0-400. PAN0-1000 has the highest
 222 conductivity with the value of $476.2 \mu\text{S cm}^{-1}$, which indicates that the graphitization degree
 223 increases with the carbonization temperature from 700 to 1000 °C. However, the GCNFs
 224 have small specific surface area. In order to increase the specific surface area of graphitized
 225 carbon nanofibers, the carbon nanofibers are continually calcinated at 400 °C under air
 226 atmosphere. Fig. 2(A) shows the nitrogen adsorption-desorption isotherms of PAN0-1000

227 and PAN0-400. The BET specific surface areas of PAN0-1000 and PAN0-400 are calculated
 228 to be 40.6 and 542.6 $\text{m}^2 \text{g}^{-1}$, respectively. After further calcination at 400 °C in air, the
 229 specific surface area of PAN0-400 increased 12.4 times than that of PAN0-1000. Fig. 2(B)
 230 displays the distributions of the pore size of PAN0-1000 and PAN0-400. Most pore diameter
 231 of PAN0-1000 ranges from 15 to 50 nm and a main peak centers at ~22 nm. The pore
 232 diameter of PAN0-400 has relatively large variation range of 3.5 – 50 nm. Most pore
 233 diameter of PAN0-400 ranges from 3.5 to 23 nm and a main peak centers at ~6.4 nm. As
 234 shown in Table 2, it is worth noting that the conductivity of PAN0-400 is also much higher
 235 than PAN0-250 calcinating at 700 °C (PAN0-700). The method will be applied in the
 236 preparation of the follow-up composite of nanofibers in this paper.



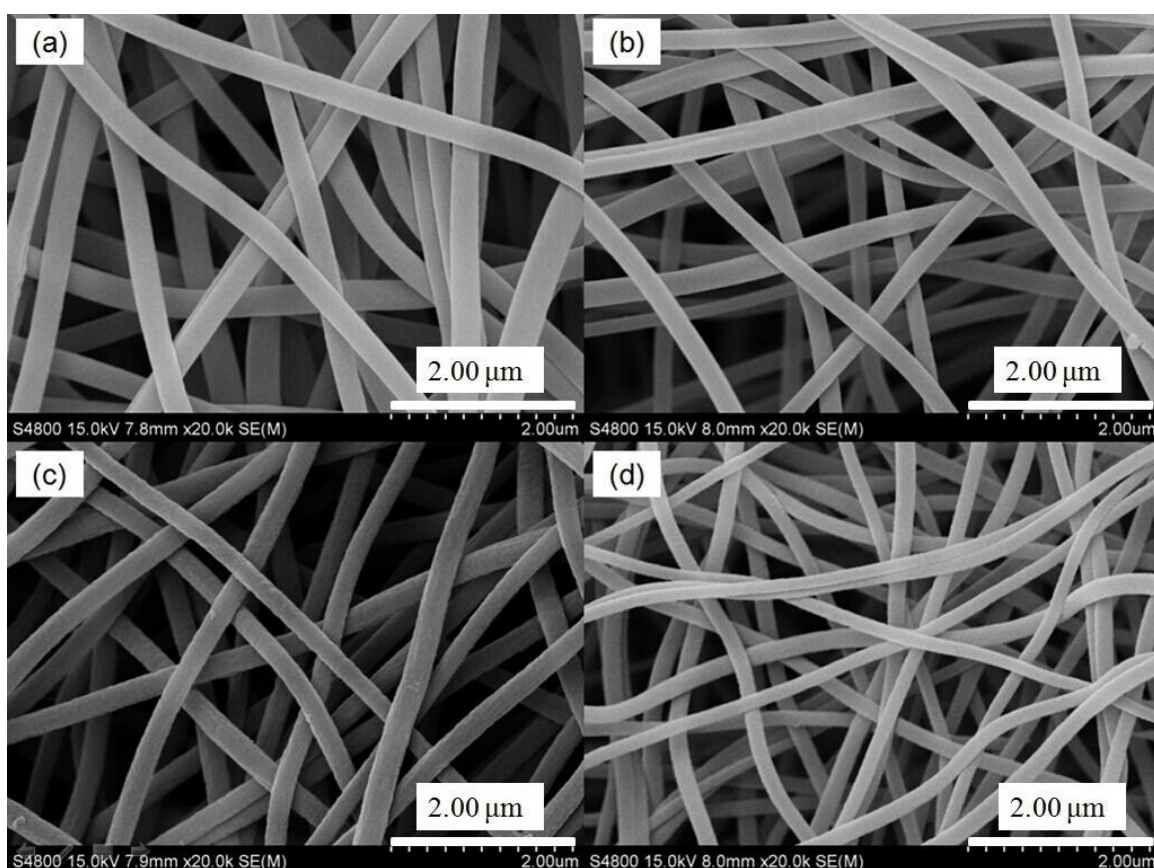
237
 238 **Fig. 2** Nitrogen adsorption-desorption isotherms of PAN0-1000 and PAN0-400 (A) and and
 239 pore size distributions of PAN0-1000 and PAN0-400 (B).

240 **Table 2** Conductivity of carbon nanofibers in different calcinating process and BET test
 241 results.

Samples	PAN0-700	PAN0-900	PAN0-1000	PAN0-400
Conductivity ($\mu\text{S cm}^{-1}$)	1.1	217.4	476.2	37.5
BET ($\text{m}^2 \text{g}^{-1}$)	—	—	40.6	542.6

245 The morphology and the diameter of the electrospun nanofibers of PAN0 and PAN3 are
 246 compared. It is found that there is no distinct difference between pure PAN nanofibers and

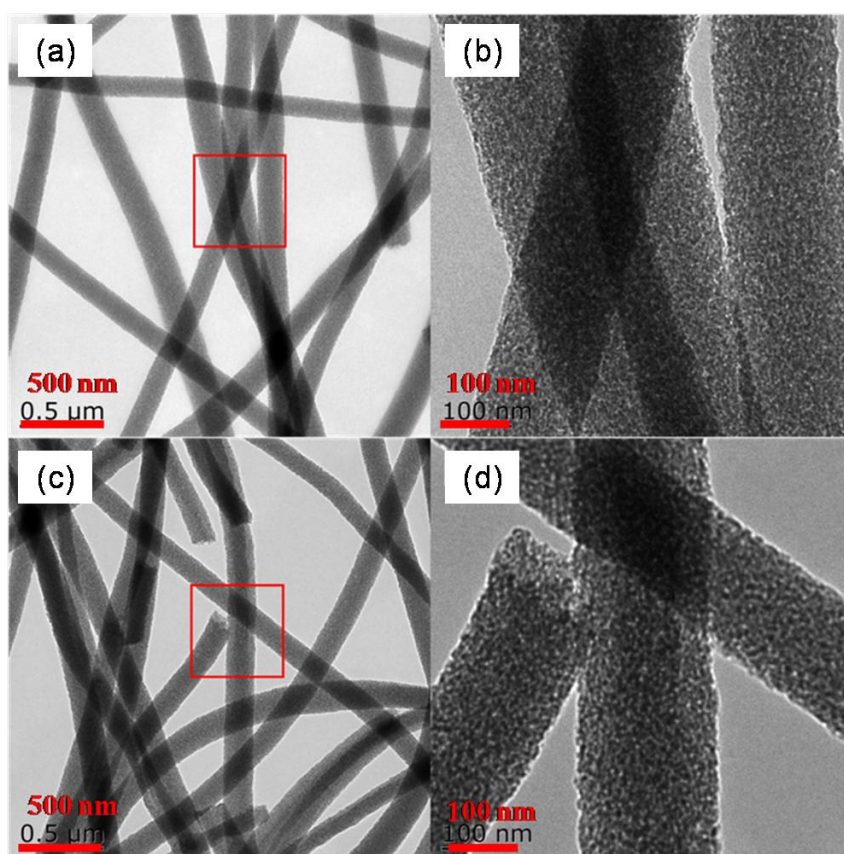
247 composite nanofibers as shown in Fig. S1, indicating that the electrospinning solution
248 together with operation conditions of electrospinning in this experiment are appropriate to
249 obtain uniform and perfect nanofibers. Fig. 3 shows SEM images of PAN3-250, PAN3-1000,
250 PAN3-400 and PAN3-500. All nanofibers exhibit homogeneously distributed diameters. Fig.
251 S2 shows the diameter distributions of PAN3-400 and PAN3-500. The mean sizes of of
252 PAN3-400 and PAN3-500 are 250 and 160 nm, respectively. More interesting, when the
253 carbon nanofibers was successively calcinated at 500 °C under Ar atmosphere, the average
254 diameter of PAN3-500 decreased obviously comparing with that of PAN3-400, which was
255 due to the consumption of carbon in ferric iron reduction reaction. In the control experiment,
256 the average diameter of PAN0-500 has no distinct decrease relative to that of PAN0-400 as
257 shown in Fig. S3.



258 **Fig. 3** SEM images of PAN3-250 (a), PAN3-1000 (b), PAN3-400 (c) and PAN3-500 (d).
259

260 As shown in Fig. 4(a) and (c), PAN3-400 and PAN3-500 have homogeneous

261 morphologies. But the porosities are distinctly increasing along with continuous calcination.
262 As can be seen from Fig. 4(b) and (d), there are many tiny pores and particles in PAN3-400
263 and PAN3-500. The portion of darker colour of PAN3-400 and PAN3-500 would be iron
264 oxides nanoparticles. The lighter colour would be carbon and tiny pores of them. The little
265 white spots should be pores. The above-mentioned iron oxides nanoparticles, carbon and
266 pores can be certified by following XRD patterns in Fig. 8(A), Raman spectra in Fig. 8(E)
267 and BET values in Table.2, respectively. What should be noted is that in the third calcination
268 process, both the flow of air and the placed apparatuses of PAN3-1000 have great influence
269 to integral morphology of nanofiber and respective content of carbon and iron oxides. Fig. S4
270 shows two different equipments in the third calcination process. Fig. 5 shows the SEM and
271 TEM images of product calcinated using apparatus in Fig. S4(b) in the third calcinating
272 process. Fig. 5(a) and Fig. 5(b) have obvious different morphologies comparing with Fig. 3(c)
273 and Fig. 4(b), respectively. The degree contacting with air of PAN3-1000 in the third
274 calcination process is responsible for the results. What's more, large percentage shrinkage in
275 area would occur or red brown product would generate at much higher temperature or larger
276 flow rate of air. In this paper, the relevant experiments of a series of air flow and different
277 equipments in the third calcinating process will not be further discussed. And all of the other
278 products (PAN3-400 and PAN0-400) were calcinated using the apparatus in Fig. S4(a).

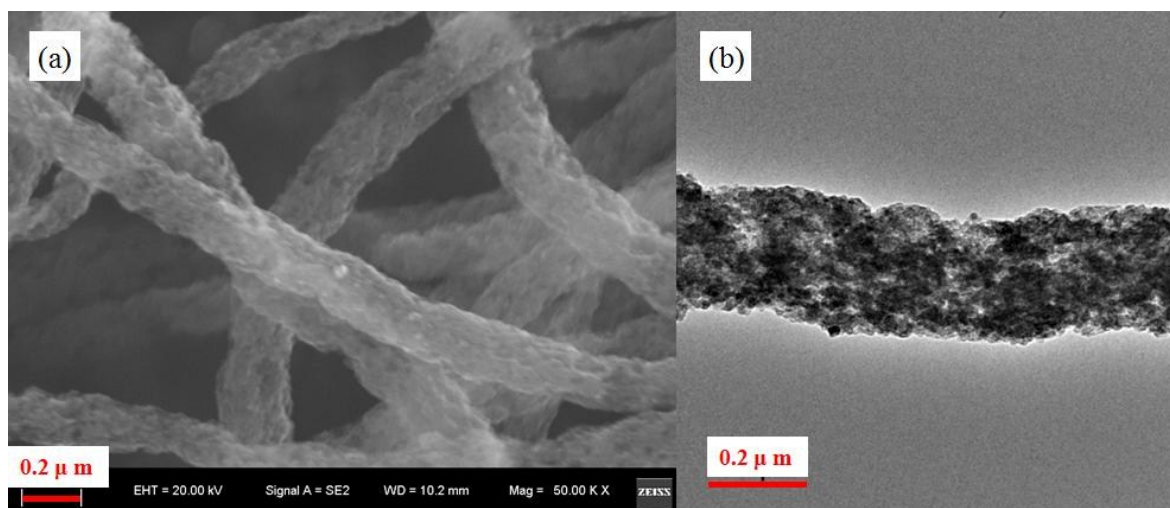


279

280 **Fig. 4** Typical TEM image of PAN3-400 (a) and its partial magnification (b), representative

281

TEM image of PAN3-500 (c) and its partial magnification (d).



282

283 **Fig. 5** SEM (a) and TEM (b) images of product using calcinating equipment in Fig. 4(b) in

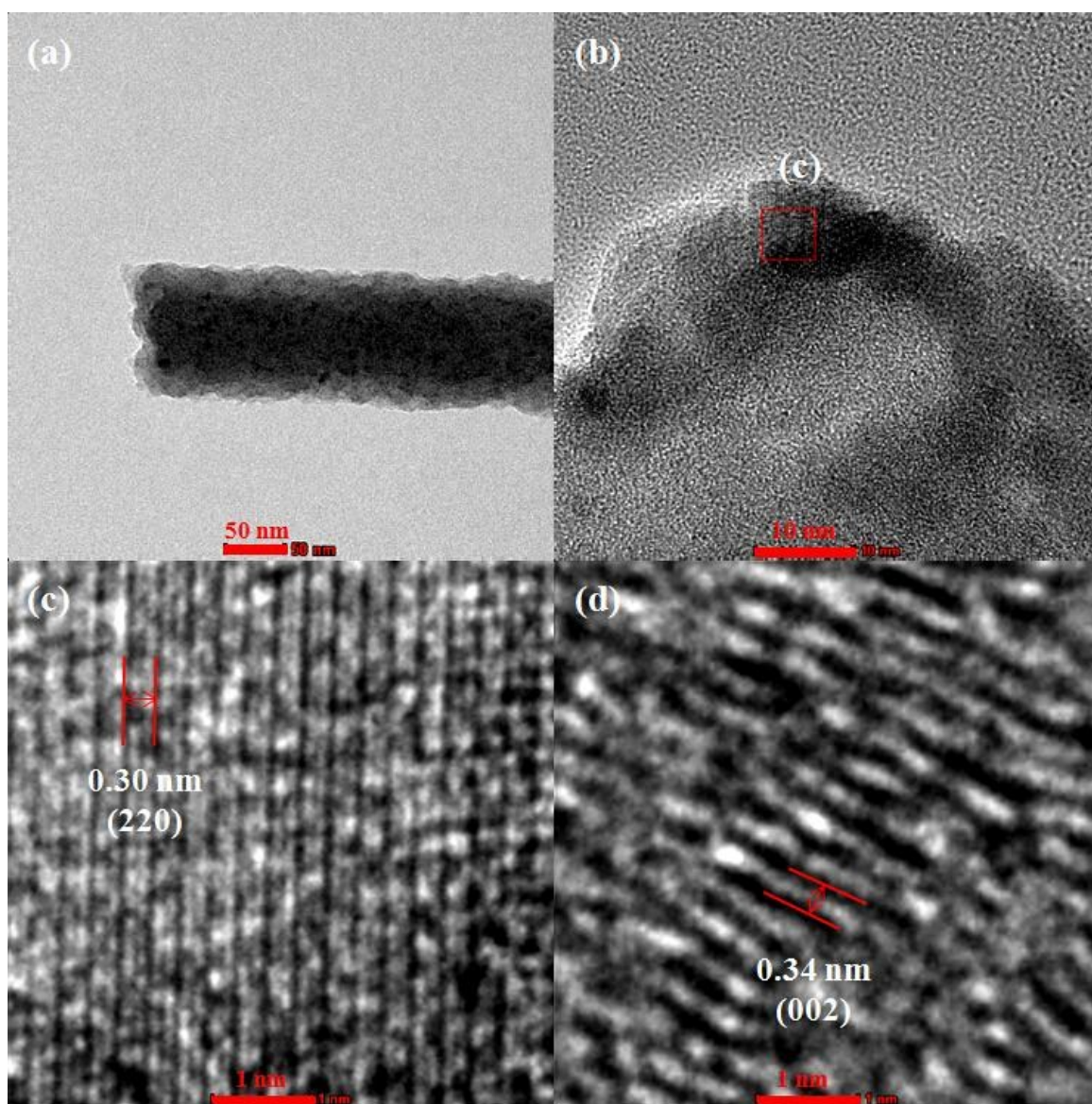
284

the third calcination process.

285

Fig. 6 shows HRTEM images of PAN3-500. The clear shell lattice fringes with

286 d-spacing of 0.30 nm in HRTEM picture (Fig. 6(c)) shows are in good agreement with that of
287 (220) plane of cubic Fe_3O_4 . Fig. 6(d) demonstrates the clear shell lattice fringes with average
288 d-spacing of 0.34 nm, corresponding to the (002) plane of hexagonal graphite. But the
289 lattice structures are seldom observed. As shown in table 2, the conductivity of PAN0-400 is
290 reduced significantly comparing with PAN0-1000. The lattice structures of graphitized
291 carbon nanofibers would have been destroyed to a great extent in the calcination processes at
292 400 °C in air for 3 h and carbon thermal reduction at 500 °C for 2 h.



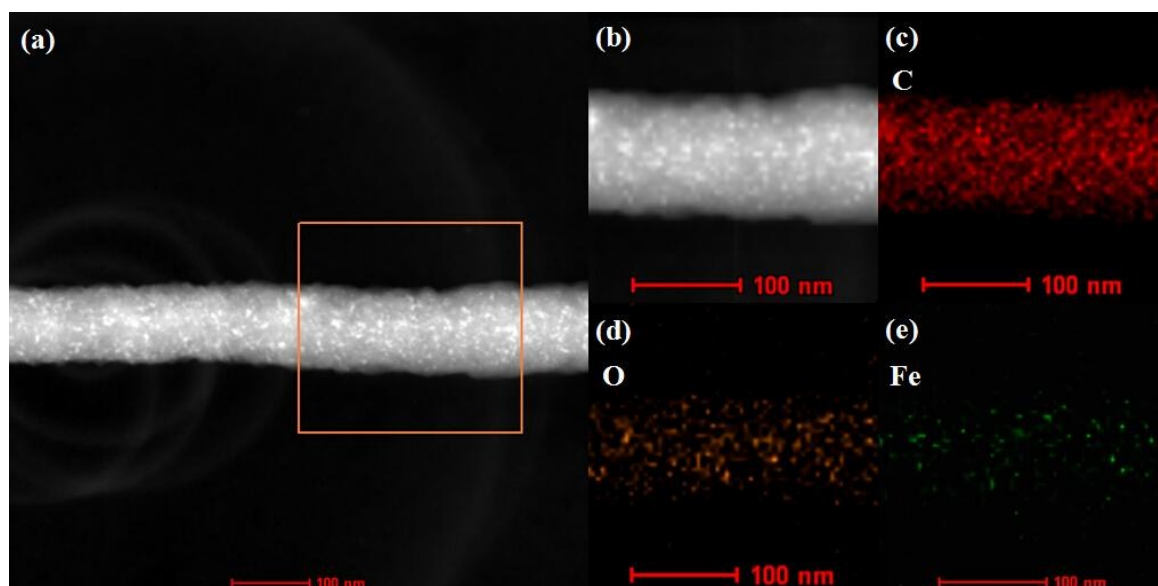
293

294

Fig. 6 Typical structure of PAN3-500 (a), partial enlargement of a cross-section of

295 PAN3-500 (b), the boxed region of part (b) - the observed crystallites in the HRTEM image
 296 corresponding to Fe_3O_4 (c), and seldom observed HRTEM image of lattice structure porous
 297 carbon of PAN3-500 (d).

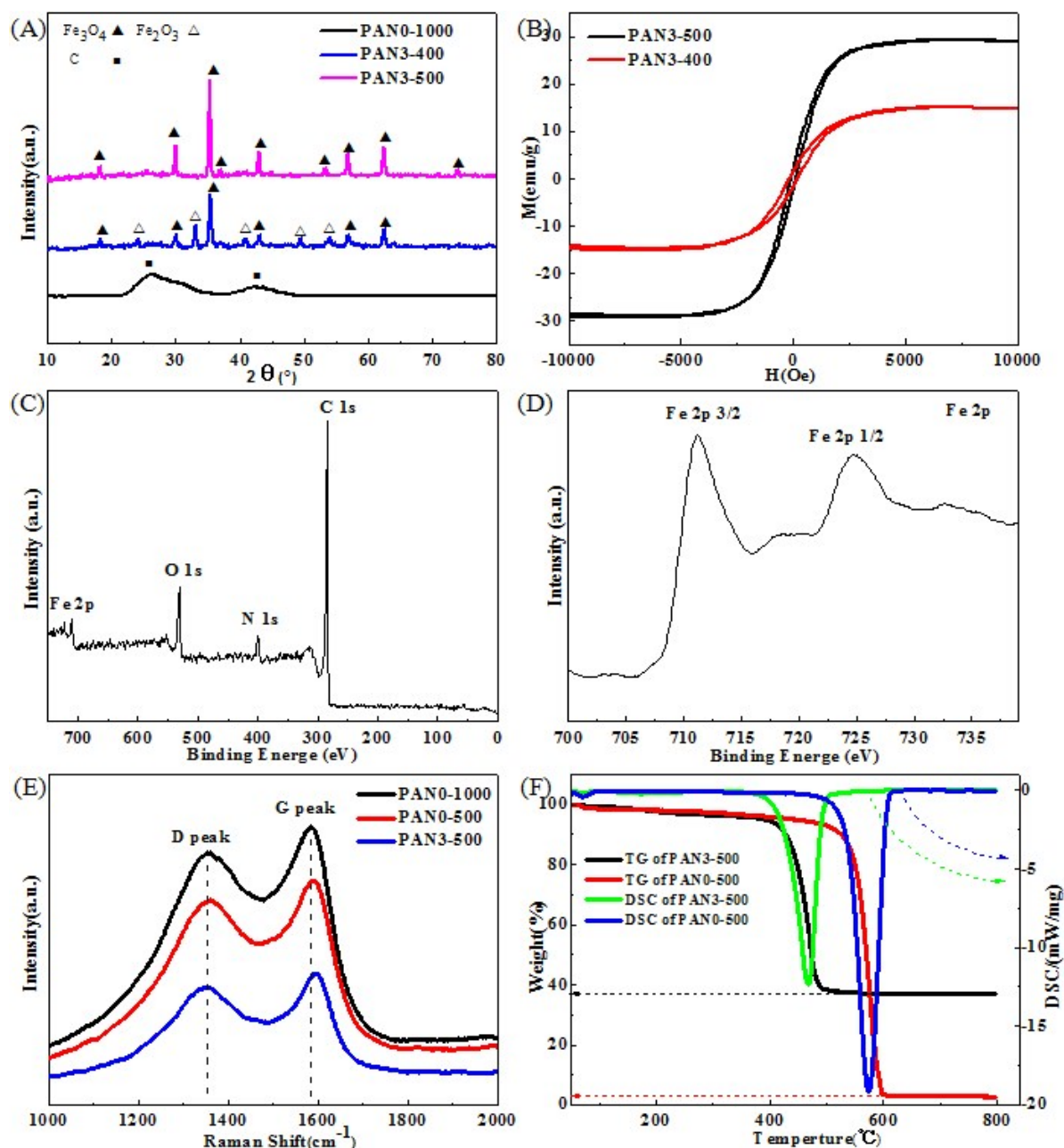
298 The PAN3-500 composites are expressed by the element maps from EDX spectroscopy.
 299 The distributions of C, O and Fe are shown in Fig. 7(c), (d) and (e), respectively. The Fe and
 300 O elements prove the existence of iron oxide. All elements distribute uniformly in the
 301 nanofiber. Therefore, the element maps of EDX confirm the composition of PAN3-500
 302 composites.



303
 304 **Fig. 7** HAADF-STEM images of PAN3-500 (a) and partial enlargement (b), element
 305 mapping of C (c), O (d) and Fe (e).

306 Fig. 8(A) shows the XRD patterns of PAN0-1000, PAN3-400 and PAN3-500. The
 307 identified diffraction peaks of PAN0-1000 nanofibers can be clearly assigned to the
 308 hexagonal graphite (JCPDS, card 41-1487). The peak at $2\theta = 26.38$ can be indexed to (002)
 309 lattice plane of hexagonal graphite, which manifests the precursor-PAN has changed into
 310 high conductive graphitic carbon. The peaks at $2\theta = 24.14, 33.15, 35.61, 40.85, 49.48,$

311 54.09, 62.45 and 63.99 can be indexed to (012), (104), (110), (113), (024), (116), (214) and
312 (300) lattice planes of hexagonal Fe_2O_3 (JCPDS, card 33-0664), respectively. The peaks at
313 $2\theta = 18.27, 30.10, 35.42, 43.05, 56.94$ and 62.52 can be indexed to (220), (311), (400),
314 (511) and (440) lattice planes of cubic Fe_3O_4 (JCPDS, card 19-0629), respectively. In order
315 to obtain the pure Fe_3O_4 in the nanofibers, PAN3-400 composites were calcinated at $500\text{ }^\circ\text{C}$
316 in Ar. Under inert atmosphere, carbon is used as reductive agent and Fe_2O_3 transforms into
317 Fe_3O_4 . No impurity peaks from other iron oxide are observed, implying the high purity of
318 Fe_3O_4 in the nanofibers. The intense diffraction peaks of Fe_3O_4 in PAN3-500 demonstrate
319 the better crystal forms of Fe_3O_4 than that in PAN3-400. But the strong diffraction peak of
320 graphitized carbon is disappeared in XRD patterns of PAN3-400 and PAN3-500, which
321 indicates the structures of graphitized carbon have been destroyed to a great degree. The
322 hysteresis curves of as-prepared PAN3-400 and PAN3-500 are shown in Fig. 8(B). The
323 saturated magnetizations of PAN3-400 and PAN3-500 are about 15.0 and 29.2 emu g^{-1} ,
324 respectively. The results of hysteresis curves are consisted with their compositions shown
325 by XRD results. The surface electronic state and composition of PAN3-500 were further
326 investigated by XPS analysis as presented in Fig. 8(C) and (D). Fig. 8(C) reveals the
327 existence of C, N, O and Fe elements in the PAN3-500. The existence of N of PAN3-500 in
328 Fig. 8(C) should be attributable to nitrogen-containing groups of PCNFs originated PAN of
329 the raw materials. Fig. 8(D) shows the high resolution of Fe 2p spectrum. The two main
330 peaks located at 711.0 and 725.7 eV correspond to Fe 2p_{3/2} and Fe 2p_{1/2}, respectively. The
331 results shown the Fe^{3+} and Fe^{2+} states were coexisted in PAN3-500, which
332 further confirmed the iron oxide in PAN3-500 is Fe_3O_4 .



333
 334 **Fig. 8** XRD patterns of PAN0-1000, PAN3-400 and PAN3-500 (A), hysteresis loops of
 335 PAN3-400 and PAN3-500 (B), XPS survey spectrum of PAN3-500 (C) and high resolution of
 336 Fe 2p spectrum (D), Raman spectra of PAN0-1000, PAN0-500 and PAN3-500 (E), and
 337 TG-DSC curves of PAN0-500 and PAN3-500 (F).

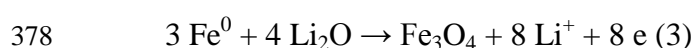
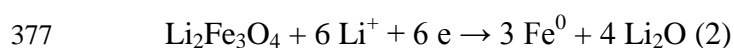
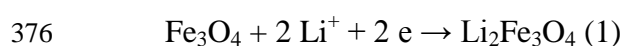
338 Fig. 8(E) shows the Raman spectra of PAN0-1000, PAN0-500 and PAN3-500. All
 339 samples show strong D (disorder) peak at about 1360 cm^{-1} and G (graphite) peak at about
 340 1590 cm^{-1} . The intensity ratios $R (I_D/I_G)$ of PAN0-1000, PAN0-500 and PAN3-500 are 0.96,

341 0.99 and 0.99, respectively. The large values of R indicate the degrees of disordered and
342 defected carbon. From Fig. 8(F), the differential scanning calorimetry (DSC) and
343 thermogravimetry (TG) curves of PAN0-500 indicate that the reaction is exothermic and the
344 loss weight is mainly between 550 °C and 600 °C. But the TG curve of PAN3-500 reveals that
345 the weight loss is mainly at the temperature range of 400 °C - 490 °C. It can be speculated
346 that the graphitized carbon structures of PAN3-500 are destroyed more seriously
347 than PAN0-500 due to the reaction of Fe₂O₃ and carbon etc. and the exothermic reaction of
348 Fe₃O₄ oxidizing into Fe₂O₃ promotes the oxidation reaction of porous carbon at the lower
349 temperature. The residual proportion of PAN3-500 is 36.9 wt. %. According to the results of
350 TGA tests, the original percentages in weight of carbon and Fe₃O₄ in PAN3-500 are
351 calculated to be 66.0 wt. % and 34.0 wt. %, respectively.

352 **Electrochemical Performance**

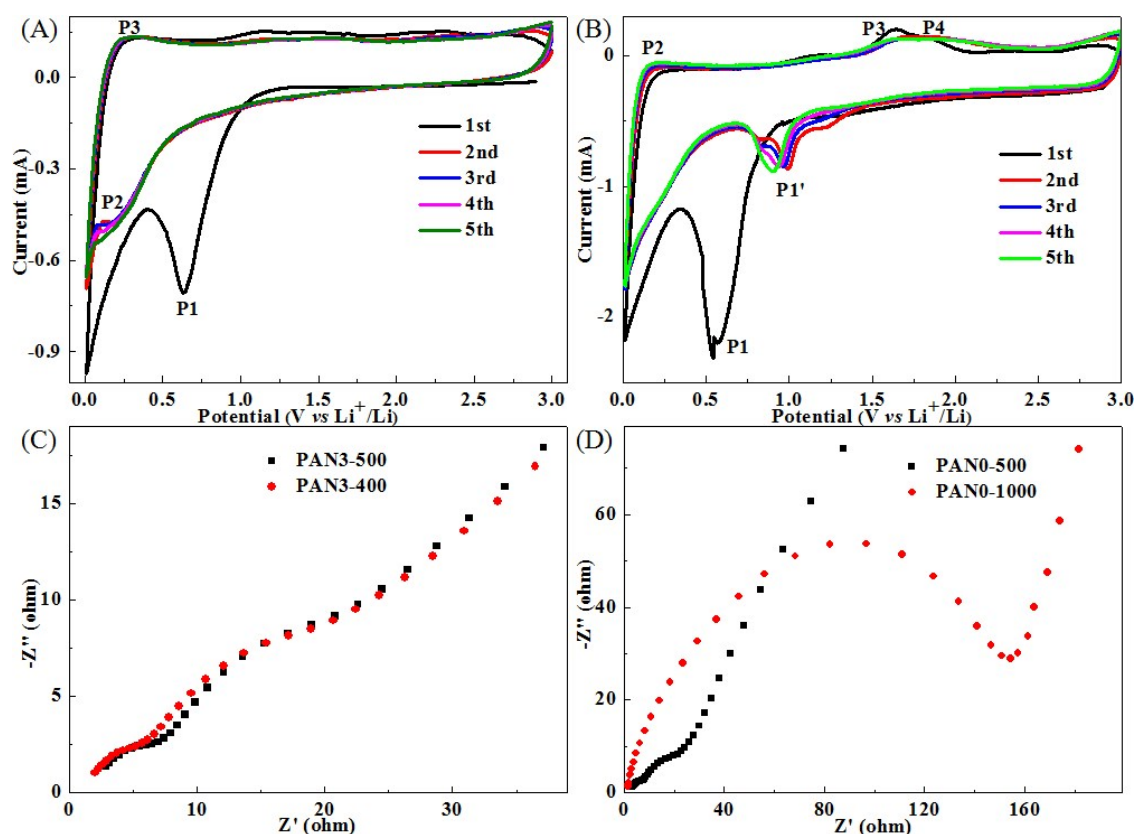
353 Porous carbon in the final mat PAN3-500 is sufficient to form a stable framework. So
354 the PAN3-500 mat has very good flexibility, as shown in Fig. S5. The CV measurements
355 were carried out to investigate the electrochemical reactions of PAN3-500 in the range of 3.0
356 to 0.01 V at a scan rate of 0.1 mV s⁻¹ at room temperature. It is seen in Fig. 9(A) the
357 PAN0-500 exhibits a cathodic peak at about 0.63 V which represents the formation of SEI
358 film and the decomposition of the electrolyte^[46] and two broad anodic peaks at about 1.16 V
359 and 2.11 V attributing to irreversible reactions with electrolyte. In the subsequent cycles, the
360 peak P2 at about 0.18 V and the peak P3 at about 0.25 V should be the insertion and
361 extraction of lithium ion from the graphitized structures of porous carbon nanofibers,
362 respectively. And the peak P1 at about 0.63 V disappears, indicating the stable and complete

363 SEI film has formed on the surface of carbon. As shown in Fig. 9(B), at the first cycle,
 364 PAN3-500 electrode exhibits a clear cathodic peak. The peak P1 at about 0.54 V might be the
 365 initial lithium insertion into the Fe_3O_4 to form $\text{Li}_2\text{Fe}_3\text{O}_4$, given by Eqn (1) ^[33,47] and the
 366 reduction reaction of $\text{Li}_2\text{Fe}_3\text{O}_4$ to Fe^0 , along with the formation of amorphous Li_2O , given by
 367 Eqn (2), as well as the formation of SEI film ^[33,41,47] and the decomposition of the electrolyte.
 368 The peak P2 should be the extraction of lithium ion from the graphitized structures of porous
 369 carbon nanofibers and the peak at about 1.20 V should be irreversible reactions with
 370 electrolyte like as the peak at about 1.16 V of PAN0-500 in Fig. 9(A). The continuous broad
 371 peaks P3 and P4 at about 1.64 V and 1.82 V are the oxidation reactions of Fe^0 to Fe^{2+} and
 372 Fe^{2+} to Fe^{3+} , respectively ^[33,36,47]. The two electrochemical reactions of Fe^0 to Fe^{2+} and Fe^{2+} to
 373 Fe^{3+} owning nearby peak potentials and the irreversible reactions could be responsible for the
 374 phenomenon that the peaks P3 and P4 merged into a more broaden peak in the subsequent
 375 cycles. The total reaction is given by Eqn (3) ^[33,41,47].



379 EIS measurements were carried out at open circuit potential with an AC voltage
 380 amplitude of 5.0 mV in a frequency range from 100 kHz to 0.01 Hz to understand the
 381 electrochemical performance of PAN3-500 comparison with PAN3-400, PAN0-500 and
 382 PAN0-1000. Fig. 9(C) and (D) display the Nyquist plots of PAN3-500 and PAN3-400
 383 electrodes, PAN0-1000 and PAN0-500 electrodes after 1 cycle at 0.5 A g^{-1} . From Fig. 9(C),
 384 the Nyquist plots of PAN3-500 and PAN3-400 have similar profiles, which are consisted of
 385 two semicircles, as well as a line, respectively. The two semicircles and the line from high
 386 frequency to low frequency were related to the resistance of SEI, charge-transfer resistance

387 on the electrolyte/electrode interface and the solid-state diffusion resistance of Li ion in the
388 electrode, respectively^[13,15]. From Fig. 9(D), it clearly shows that the radius of the semicircle
389 for PAN0-500 in the medium frequency region is much smaller than that of PAN0-1000,
390 indicating the porous structured PAN0-500 has much lower electron-transfer resistance than
391 graphitized PAN0-1000. The PAN3-500, PAN3-400 and PAN0-500 electrodes have
392 remarkably small electron-transfer resistance compared with that of PNO-1000. The results
393 indicates the greatly diminutive charge-transfer resistance at the electrode/electrolyte
394 interface should be due to the porous structure in PCNFs of PAN3-500, PAN3-400 and
395 PAN0-500, which can greatly improve the diffusion of lithium ions as well as the transfer of
396 electrons for better electrochemical performance^[12-16].



397

398 **Fig. 9** CV measurements of PAN0-500 (A), PAN3-500 (B) cycled between 0.01 and 3 V at

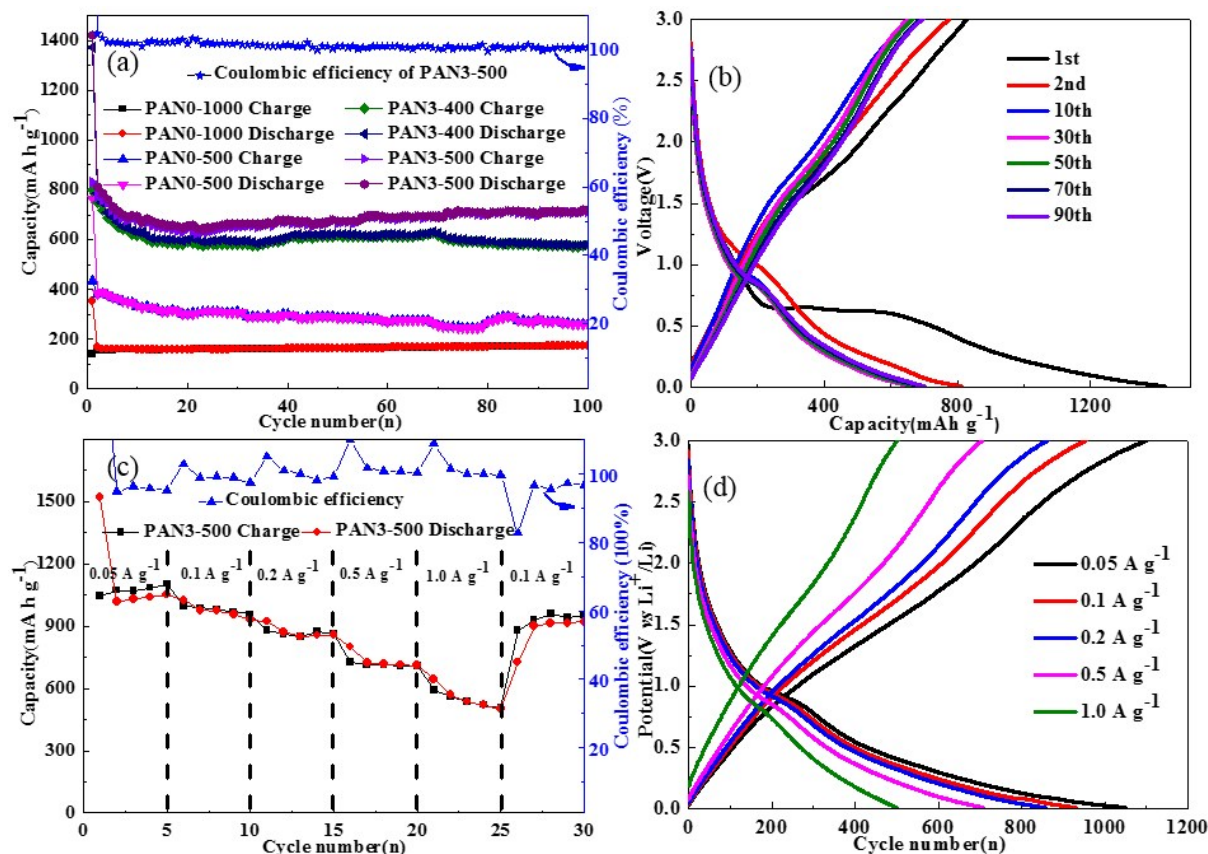
399 a scan rate of 0.1 mV s⁻¹, Nyquist plots of PAN3-500 and PAN3-400 (C), PAN0-500 and

400

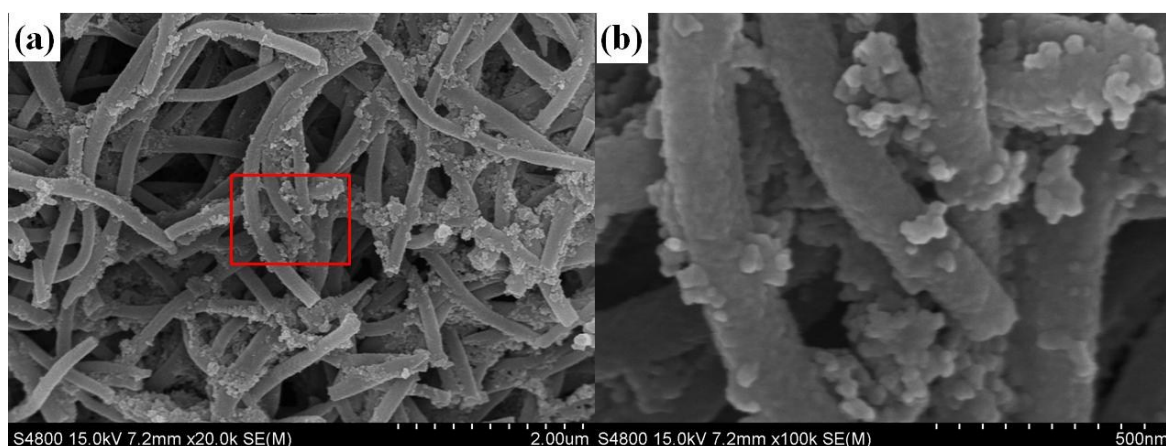
PAN0-1000 (D).

401 As the proportion of graphitized carbon in PAN3-500 is 66.0 wt. %, the specific
402 capacitance of the composites is calculated as approximate 560 mA h g^{-1} based on the
403 theoretical capacities of Fe_3O_4 926 mA h g^{-1} and graphite 372 mA h g^{-1} . Fig. 10(a) shows the
404 charge-discharge cycle performance of PAN0-1000, PAN0-500, PAN3-400 and PAN3-500 at
405 0.5 A g^{-1} in the range of 3.0 to 0.01 V. In the 100th cycle, the discharge capacity of
406 PAN0-1000, PAN0-500, PAN3-400 and PAN3-500 were 173.1, 261.1, 579.3 and 717.2 mA
407 h g^{-1} , respectively. The test results show that the capacities of composite nanofibers are
408 obviously higher than that of carbon nanofibers. The high capacity of PAN3-500 is attributed
409 to superior porosity of porous carbon and carbon coating good crystallinity of Fe_3O_4 . The
410 discharge capacities of PAN3-500 in the 1st, 2nd, 10th, 30th, 50th, 70th and 90th cycles were
411 1422.1, 811.7, 672.9, 665.0, 674.6, 692.7 and 700.6 mA h g^{-1} , respectively, indicating that
412 PAN3-500 had high capacity and remarkable capacity retention. The SEM images of
413 PAN3-500 after 100 charge-discharge cycles and one discharge cycle are shown in Fig. 11.
414 And the diameter distribution of PAN3-500 after 100 charge-discharge cycles and one
415 discharge cycle is shown in Fig. S6. The mean diameter of PAN3-500 after 100
416 charge-discharge cycles and one discharge cycle is 180 nm. The results shows that the mean
417 diameter of PAN3-500 after 100 charge-discharge cycles and one discharge cycle is the same
418 as the original PAN3-500, which can demonstrate that PAN3-500 basically has no volume
419 change in the charging-discharging process at the density of 0.5 A g^{-1} . The amounts of small
420 pores which can afford space for inserted lithium should be responsible for this phenomenon.
421 Fig. 10(b) shows the detailed charge and discharge curves of PAN3-500 at different cycle
422 numbers. As shown in Fig. 10(c), the rate capabilities of PAN3-500 were investigated at
423 various rates from 0.05 to 1.0 A g^{-1} to further evaluate the electrochemical performance.
424 When the densities were 0.05, 0.1, 0.2, 0.5 and 1.0 A g^{-1} , the PAN3-500 retained high
425 specific capacities of 1050.6, 931.1, 857.0, 709.0 and $501.6 \text{ mA h g}^{-1}$ in their own 5th cycle,

426 respectively. And then back to 0.1 A g^{-1} , the capacity still achieved $919.3 \text{ mA h g}^{-1}$. Fig. 10(d)
 427 shows the charge/discharge curves of PAN3-500 at different current densities, which display
 428 approximate symmetrical shape, indicating fine reversibility of Li^+ insertion/extraction.



429
 430 **Fig. 10** The cycling performance of PAN0-1000, PAN0-500, PAN3-400 and PAN3-500 at a
 431 current density of 0.5 A g^{-1} (a) and relevant charge and discharge curves of PAN3-500 (b),
 432 charge-discharge performance of PAN3-500 at various current rates (c) and relevant charge
 433 and discharge curves (d).



434 S4800 15.0kV 7.2mm x20.0k SE(M)

2.00μm S4800 15.0kV 7.2mm x100k SE(M)

500nm

435 **Fig. 11** SEM image of PAN3-500 after 100 charge-discharge cycles and one discharge cycle
 436 (a) and relevant magnification (b).

437 It is worth noting that the electrochemical performance of PAN3-500 in this work are
 438 comparable to most of the electrospinning and calcined products, such as Fe₂O₃ nanofibers
 439 [42-43], carbon nanofibers [44-40] and iron oxides/CNFs composites [37-41] reported in previous
 440 literatures, as shown in Table 3.

441 **Table 3** Comparison of the retaining capacity of Fe_xO_y nanofibers, carbon nanofibers or
 442 Fe_xO_y/CNFs composites preparing by electrospinning.

443 Nanocomposites	Precursors	Calcination temperature	Retaining capacity
444 Fe ₂ O ₃ -carbon	PAN-Fe(acac) ₃	At 500 °C for 3h in air	820 mA h g ⁻¹ at 0.2 C [37]
445 α-Fe ₂ O ₃ -CNFs	PAN-FeCl ₃	At 600 °C for 8 h in Ar	600 mA h g ⁻¹ at 50 mA g ⁻¹ [38]
446 α-Fe ₂ O ₃ nanorods	PVP-Fe(acac) ₃	At 500 °C for 5 h in air	1095 mA h g ⁻¹ at 0.05 C [39]
447 C/Fe ₃ O ₄	PAN-Fe(acac) ₂	At 600 °C for 10 h in Ar	1096 mA h g ⁻¹ at 0.2 A g ⁻¹ [40]
448		At 700 °C for 10 h in Ar	300 mA h g ⁻¹ at 0.2 A g ⁻¹ [40]
449 Fe ₃ O ₄ @PCFs	PAN-PS-Fe ₃ O ₄	At 600 °C for 2 h in Ar	541 mA h g ⁻¹ at 2.0 A g ⁻¹ [41]
450 Hollow Fe ₂ O ₃ nanofibers	PVP-Fe(acac) ₃	At 500 °C for 4 h in air	1293 mA h g ⁻¹ at 0.06 A g ⁻¹ [42]
451 Porous Fe ₂ O ₃ nanotubes	PVP-Fe(acac) ₃	At 500 °C for 3 h in air	987.7 mA h g ⁻¹ at 0.2 A g ⁻¹ [43]
452 Carbon nanofibers	PAN	At 700 °C in Ar	275 mA h g ⁻¹ at 0.03 A g ⁻¹ [44]
453		At 1000 °C in Ar	450 mA h g ⁻¹ at 0.03 A g ⁻¹ [44]
454		At 2800 °C in Ar	140 mA h g ⁻¹ at 0.03 A g ⁻¹ [44]
455 Carbon nanofiber	PAN	At 800 °C for 1 h in Ar	407 mA h g ⁻¹ at 0.15 A g ⁻¹ [45]
456		At 1300 °C for 1 h in Ar	239 mA h g ⁻¹ at 0.15 A g ⁻¹ [45]
457 Fe ₃ O ₄ /PCNFs	PAN-Fe(acac) ₃	At 1000 °C for 2 h in Ar,	
458		at 400 °C for 3 h in Air,	579.3 mA h g ⁻¹ at 0.5 A g ⁻¹ [This]
459		at 500 °C for 2 h in Ar	717.2 mA h g ⁻¹ at 0.5 A g ⁻¹ [This]

460 Comment: PS = polystyrene, PVP = polyvinylpyrrolidone, PCFs = porous carbon fibers.

461 CONCLUSIONS

462 In summary, we synthesized Fe₃O₄/porous carbon nanofibers by electrospinning and
 463 subsequent unique calcination processes. Graphitized carbon was obtained by calcination at
 464 1000 °C in Ar. Porous structured carbon was obtained by further calcination at 400 °C in air,
 465 which had much higher porosity than graphitized carbon. Fe₃O₄/porous carbon nanofibers

466 were prepared via the carbon-thermal reduction process by the final calcination at 500 °C in
467 Ar. Porous carbon coating nano-sized Fe₃O₄ nanofibers composites had excellent
468 performance as anodes for lithium ion batteries. The reversible capacity was higher than
469 Fe_xO_y/porous carbon nanofibers composites and carbon nanofibers. Fe₃O₄/porous carbon
470 nanofibers kept a reversible capacity of 717.2 mA h g⁻¹ at 0.5 A g⁻¹ after 100 cycles. At 0.05 A
471 g⁻¹, the composites delivered a reversible capacity as high as 1050.6 mA h g⁻¹. The porous
472 carbon nanofibers of coating Fe₃O₄ nanoparticles have good conductivity, which is useful for
473 electronic transmission and fast diffusion of lithium in the charge-discharge process. What's
474 more, carbon can buffer the volume changes between nano-sized Fe₃O₄ nanoparticles and Fe
475 atoms in charging and discharging process and make the transition reactions in situ to
476 maintain the crystal structures. So the combinations of conductive porous carbon nanofibers
477 and nano-sized Fe₃O₄ are responsible for the higher capability and good cycling stability. We
478 believe much higher capacity Fe₃O₄/porous carbon nanofibers can be fabricated by more
479 appropriate calcination conditions containing calcinating apparatus, temperature and flow
480 rate of air. More importantly, the method of preparing Fe₃O₄/porous carbon nanofibers is
481 novel.

482 ASSOCIATED CONTENT

483 Supporting Information

484 Additional experimental data including SEM images of PAN0 and PAN3, SEM images
485 of PAN3-400 (a), PAN3-500 (c) and relevant diameter distributions of PAN3-400 (b),
486 PAN3-500 (d), SEM images of PAN0-400, PAN0-500 and relevant diameter distributions,
487 two different equipments in the third calcination process, picture of flexible PAN3-500
488 electrodes, SEM image of PAN3-500 after 100 charge-discharge cycles and one discharge
489 cycle and relevant diameter distribution.

490 AUTHOR INFORMATION

491 Corresponding Author *E-mail: gwldiao@yzu.edu.cn, chenming@yzu.edu.cn. Tel.:
492 +86-514-87975436. Fax:+86-514-87975244.

493 **Notes**

494 The authors declare no competing financial interest.

495 **ACKNOWLEDGMENTS**

496 The authors appreciate the Test Center of Yangzhou University for TEM and HRTEM
497 measurements and the financial support from the National Natural Science Foundation of
498 China (grant no. 21273195 and20901065), the Project Funded by the Natural Science
499 Foundation of Education Committee of Jiangsu Province (12KJB150023), the Scientific
500 Innovation Planing Program for Academic Graduates of Jiangsu Ordinary Universities
501 (KYLX_1336), the Cooperation Fund from Yangzhou Government and Yangzhou University
502 (Grant no. 2012038-9) and the Priority Academic Program Development of Jiangsu Higher
503 Education Institutions.

504 **References**

- 505 [1] Ramanathan, V.; Carmichael, G. Global and Regional Climate Changes Due to Black
506 Carbon. *Nature Geosci.*, 2008, **1**, 221-227.
- 507 [2] Ramanathan, V.; Feng, Y. Air Pollution, Greenhouse Gases and Climate Change: Global
508 and Regional Perspectives. *Environ.*, 2009, **43**, 37-50.
- 509 [3] Thackeray, M. M.; Wolverton, C.; Isaacs, E. D. Electrical Energy Storage for
510 Transportation-approaching the Limits of, and Going Beyond, Lithium-ion Batteries. *Energy*
511 *Environ. Sci.*, 2012, **5**, 7854-7863.
- 512 [4] Dresselhaus, M. S.; Thomas, I. L. Alternative Energy Technologies. *Nature*, 2001, **414**,
513 332-337.
- 514 [5] Dunn, B., Kamath, H.; Tarascon, J. M. Electrical Energy Storage for the Grid: a Battery of
515 Choices. *Science*, 2011, **334**, 928-935.

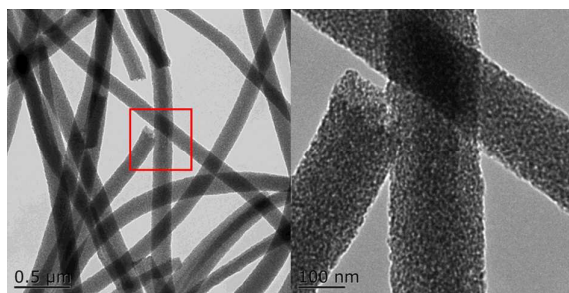
- 516 [6] Van Noorden, R. The Rechargeable Revolution: A Better Battery. *Nature*, 2014, **507**,
517 26-28.
- 518 [7] Scrosati, B.; Garche, J. Lithium Batteries: Status, Prospects and Future. *J. Power Sources*,
519 2010, **195**, 2419-2430.
- 520 [8] Kang, K.; Meng, Y. S.; Br  ger, J.; Grey, C. P.; Ceder, G. Electrodes with High Power and
521 High Capacity for Rechargeable Lithium Batteries. *Science*, 2006, **311**, 977-980.
- 522 [9] Yoshio, M.; Wang, H.; Fukuda, K.; Hara, Y.; Adachi, Y. Effect of Carbon Coating on
523 Electrochemical Performance of Treated Natural Graphite as Lithium-ion Battery Anode
524 Material. *J. Electrochem. Soc.*, 2000, **147**, 1245-1250.
- 525 [10] Yoshio, M.; Wang, H.; Fukuda, K.; Umeno, T.; Abe, T.; Ogumi, Z. Improvement of
526 Natural Graphite as a Lithium-ion Battery Anode Material, from Raw Flake to
527 Carbon-Coated Sphere. *J. Mater. Chem.*, 2004, **14**, 1754- 1758.
- 528 [11] Wu, Y. P.; Rahm, E.; Holze, R. Carbon Anode Materials for Lithium Ion Batteries. *J.*
529 *Power Sources*, 2003, **114**, 228-236.
- 530 [12] Zhang, L. S.; Fan, W. and Liu, T. X. A Flexible Free-standing Defect-rich
531 MoS₂/graphene/carbon Nanotube Hybrid Paper as a Binder-free Anode for high-performance
532 Lithium Ion Batteries. *RSC Adv.*, 2015, **5**, 43130-43140.
- 533 [13] Miao, Y. E.; Huang, Y.; Zhang, L.; Fan, W.; Lai, F. and Liu, T. Electrospun Porous
534 Carbon Nanofiber@MoS₂ Core/sheath Fiber Membranes as Highly Flexible and Binder-free
535 Anodes for Lithium-ion Batteries. *Nanoscale*, 2015, **7**(25), 11093-11101.
- 536 [14] Zhang, L. S.; Huang, Y. P.; Zhang, Y. F.; Fan, W.; Liu, T. X. Three-Dimensional
537 Nanoporous Graphene-Carbon Nanotube Hybrid Frameworks for Confinement of SnS₂
538 Nanosheets: Flexible and Binder-Free Papers with Highly Reversible Lithium Storage. *ACS*
539 *Appl. Mater. Interfaces*, 2015, **7**(50), 27823–27830.
- 540 [15] Zhang, L. S.; Huang, Y. P.; Zhang, Y. F.; Gu, H. H.; Fan, W. and Liu, T. X. Flexible

- 541 Electrospun Carbon Nanofiber@NiS Core/Sheath Hybrid Membranes as Binder-Free Anodes
542 for Highly Reversible Lithium Storage. *Adv. Mater. Interfaces*, 2016, DOI:
543 10.1002/admi.201500467.
- 544 [16] Zhang, L. S.; Fan, W.; Tjiu, W. W. and Liu, T. X. 3D Porous Hybrids of Defect-rich
545 MoS₂/graphene Nanosheets with Excellent Electrochemical Performance as Anode Materials
546 for Lithium Ion Batteries. *RSC Adv.*, 2015, **5**, 34777-34787.
- 547 [17] Poizot, P.; Laruelle, S.; Grugeon, S.; Dupont, L.; Tarascon, J. M. Nano-sized
548 Transition-metal Oxides as Negative-electrode Materials for Lithium-ion Batteries. *Nature*,
549 2000, **407**, 496-499.
- 550 [18] Armstrong, M. J.; O'Dwyer, C.; Macklin, W. J.; Holmes, J. D. Evaluating the
551 Performance of Nanostructured Materials as Lithium-ion Battery electrodes. *Nano Res.*, 2014,
552 **7**, 1-62.
- 553 [19] Wu, H.B.; Chen, J.S.; Hng, H.H.; Lou, X.W. Nanostructured Metal Oxide-based
554 Materials as Advanced Anodes for Lithium-ion Batteries. *Nanoscale*, 2012, **4**, 2526-2542.
- 555 [20] Zhang, L.; Wu, H. B.; Lou, X. W. Iron-oxide-based Advanced Anode Materials for
556 Lithium-ion Batteries. *Adv. Energy Mater.*, 2014, **4**, 1032-1039.
- 557 [21] Arico, A. S.; Bruce, P.; Scrosati, B.; Tarascon, J. M.; Van Schalkwijk, W. Nanostructured
558 Materials for Advanced Energy Conversion and Storage Devices. *Nature Mater.*, 2005, **4**,
559 366- 377.
- 560 [22] Zhu, T.; Chen, J. S.; Lou, X. W. Glucose-assisted One-pot Synthesis of FeOOH
561 Nanorods and Their Transformation to Fe₃O₄@ Carbon Nanorods for Application in Lithium
562 Ion Batteries. *J. Phys. Chem. C*, 2011, **115**, 9814-9820.
- 563 [23] Jin, S.; Deng, H.; Long, D.; Liu, X.; Zhan, L.; Liang, X.; et al. Facile Synthesis of
564 Hierarchically Structured Fe₃O₄/carbon Micro-flowers and Their Application to Lithium-ion
565 Battery Anodes. *J. Power Sources*, 2011, **196**, 3887-3893.

- 566 [24] Yoon, T.; Chae, C.; Sun, Y. K.; Zhao, X.; Kung, H. H.; Lee, J. K. Bottom-up in situ
567 Formation of Fe₃O₄ Nanocrystals in a Porous Carbon Foam for Lithium-ion Battery
568 Anodes. *J. Mater. Chem.*, 2011, **21**, 17325- 17330.
- 569 [25] Lee, J. E.; Yu, S. H.; Lee, D. J.; Lee, D. C.; Han, S. I.; Sung, Y. E.; et al. Facile and
570 Economical Synthesis of Hierarchical Carbon-coated Magnetite Nanocomposite Particles and
571 Their Applications in Lithium Ion Battery Anodes. *Energy Environ. Sci.*, 2012, **5**, 9528-9533.
- 572 [26] Zhou, G.; Wang, D. W.; Hou, P. X.; Li, W.; Li, N.; Liu, C.; et al. A Nanosized Fe₂O₃
573 Decorated Single-walled Carbon Nanotube Membrane as a High-performance Flexible
574 Anode for Lithium Ion Batteries. *J. Mater. Chem.*, 2012, **22**, 17942-17946.
- 575 [27] Chou, S. L.; Wang, J. Z.; Wexler, D.; Konstantinov, K.; Zhong, C.; Liu, H. K.; et al.
576 High-surface-area α -Fe₂O₃/Carbon Nanocomposite: One-step Synthesis and its Highly
577 Reversible and Enhanced High-rate Lithium Storage Properties. *J. Mater. Chem.*, 2010, **20**,
578 2092-2098.
- 579 [28] Li, Y.; Zhu, C.; Lu, T.; Guo, Z.; Zhang, D.; Ma, J.; et al. Simple Fabrication of a
580 Fe₂O₃/Carbon Composite for Use in a High-performance Lithium Ion Battery. *Carbon*, 2013,
581 **52**, 565-573.
- 582 [29] Lv, P.; Zhao, H.; Zeng, Z.; Wang, J.; Zhang, T.; Li, X. Facile Preparation and
583 Electrochemical Properties of Carbon Coated Fe₃O₄ as Anode Material for Lithium-ion
584 Batteries. *J. Power Sources*, 2014, **259**, 92-97.
- 585 [30] Zeng, Z.; Zhao, H.; Wang, J.; Lv, P.; Zhang, T.; Xia, Q. Nanostructured Fe₃O₄@C as
586 Anode Material for Lithium-ion Batteries. *J. Power Sources*, 2014, **248**, 15-21.
- 587 [31] Muraliganth, T.; Murugan, A. V.; Manthiram, A. Facile Synthesis of Carbon-decorated
588 Single-crystalline Fe₃O₄ Nanowires and their Application as High Performance Anode in
589 Lithium Ion Batteries. *Chem. Commun.*, 2009, **47**, 7360-7362.
- 590 [32] Wu, Y.; Wei, Y.; Wang, J.; Jiang, K.; Fan, S. Conformal Fe₃O₄ Sheath on Aligned Carbon

- 591 Nanotube Scaffolds as High-performance Anodes for Lithium Ion Batteries. *Nano Lett.*, 2013,
592 **13**, 818-823.
- 593 [33] He, C.; Wu, S.; Zhao, N.; Shi, C.; Liu, E.; Li, J. Carbon-encapsulated Fe₃O₄
594 Nanoparticles as a High-rate Lithium Ion Battery Anode Material. *ACS Nano*, 2013, **7**,
595 4459-4469.
- 596 [34] Su, Y.; Li, S.; Wu, D.; Zhang, F.; Liang, H.; Gao, P.; et al. Two-dimensional
597 Carbon-coated Graphene/metal Oxide Hybrids for Enhanced Lithium Storage. *ACS Nano*,
598 2012, **6**, 8349-8356.
- 599 [35] Yoon, T.; Chae, C.; Sun, Y. K.; Zhao, X.; Kung, H. H.; Lee, J. K. Bottom-up in situ
600 Formation of Fe₃O₄ Nanocrystals in a Porous Carbon Foam for Lithium-ion Battery
601 Anodes. *J. Mater. Chem.*, 2011, **21**, 17325-17330.
- 602 [36] Kang, E.; Jung, Y. S.; Cavanagh, A. S.; Kim, G. H.; George, S. M.; Dillon, A. C.; et al.
603 Fe₃O₄ Nanoparticles Confined in Mesocellular Carbon Foam for High Performance Anode
604 Materials for Lithium-ion Batteries. *Adv. Funct. Mater.*, 2011, **21**, 2430-2438.
- 605 [37] Zhang, X.; Liu, H.; Petnikota, S.; Ramakrishna, S.; Fan, H. J. Electrospun Fe₂O₃-carbon
606 Composite Nanofibers as Durable Anode Materials for Lithium Ion Batteries. *J. Mater. Chem.*
607 *A*, 2014, **2**, 10835-10841.
- 608 [38] Ji, L.; Toprakci, O.; Alcoutlabi, M.; Yao, Y.; Li, Y.; Zhang, S.; et al. α -Fe₂O₃
609 Nanoparticle-loaded Carbon Nanofibers as Stable and High-capacity Anodes for
610 Rechargeable lithium-ion Batteries. *ACS Appl. Mater. Interfaces*, 2012, **4**, 2672-2679.
- 611 [39] Cherian, C. T.; Sundaramurthy, J.; Kalaivani, M.; Ragupathy, P.; Kumar, P. S.; Thavasi,
612 V.; et al. Electrospun α -Fe₂O₃ Nanorods as a Stable, High Capacity Anode Material for Li-ion
613 Batteries. *J. Mater. Chem.*, 2012, **22**, 12198-12204.
- 614 [40] Wang, L.; Yu, Y.; Chen, P. C.; Zhang, D. W.; Chen, C. H. Electrospinning Synthesis of
615 C/Fe₃O₄ Composite Nanofibers and Their Application for High Performance Lithium-ion

- 616 Batteries. *J. Power Sources*, 2008, **183**, 717-723.
- 617 [41] Qin, X.; Zhang, H.; Wu, J.; Chu, X.; He, Y. B.; Han, C.; et al. Fe₃O₄ Nanoparticles
618 Encapsulated in Electrospun Porous Carbon Fibers with a Compact Shell as
619 High-performance Anode for Lithium Ion Batteries. *Carbon*, 2015, **87**: 347-356.
- 620 [42] Chaudhari, S.; Srinivasan, M. 1D Hollow α -Fe₂O₃ Electrospun Nanofibers as High
621 Performance Anode Material for Lithium Ion Batteries. *J. Mater. Chem.*, 2012, **22**,
622 23049-23056.
- 623 [43] Wang, H. G.; Zhou, Y.; Shen, Y.; Li, Y.; Zuo, Q.; Duan, Q. Fabrication, Formation
624 Mechanism and the Application in Lithium-ion Battery of Porous Fe₂O₃ Nanotubes Via
625 Single-spinneret Electrospinning. *Electrochim. Acta*, 2015, **158**: 105-112.
- 626 [44] Kim, C.; Yang, K. S.; Kojima, M.; Yoshida, K.; Kim, Y. J.; Kim, Y. A.; et al.
627 Fabrication of Electrospinning-derived Carbon Nanofiber Webs for the Anode Material of
628 Lithium-ion Secondary Batteries. *Adv. Funct. Mater.*, 2006, **16**, 2393-2397.
- 629 [45] Peng, Y. T.; Lo, C. T. Effect of Microstructure and Morphology of Electrospun
630 Ultra-small Carbon Nanofibers on Anode Performances for Lithium Ion
631 Batteries. *J. Electrochem. Soc.*, 2015, **162**, A1085-A1093.
- 632 [46] Chen, M.; Yu, C.; Liu, S.; Fan, X.; Zhao, C.; Zhang, X.; Qiu, J. Micro-sized Porous
633 Carbon Spheres with Ultra-high Rate Capability for Lithium Storage. *Nanoscale*, 2015, **7**,
634 1791-1795.
- 635 [47] Wang, J. Z.; Zhong, C.; Wexler, D.; Idris, N. H.; Wang, Z. X.; Chen, L. Q.; Liu, H.K.
636 Graphene-encapsulated Fe₃O₄ Nanoparticles with 3D Laminated Structure as Superior Anode
637 in Lithium Ion Batteries. *Chem.-Eur. J.*, 2011, **17**, 661-667.



Ferroferric oxide/porous carbon nanofibers composites were synthesized by electrospinning and subsequent innovative thermal treatments, exhibiting enhanced electrochemical performance.